Journal of Materials Chemistry A

PAPER

View Article Online
View Journal | View Issue

Cite this: J. Mater. Chem. A, 2016, 4, 4755

Ultrafast laser-assisted synthesis of hydrogenated molybdenum oxides for flexible organic solar cells†

Wan Jae Dong, Juyoung Ham, Gwan Ho Jung, Jun Ho Son and Jong-Lam Lee*

A novel method to synthesize a hydrogenated molybdenum oxide (H_yMoO_{3-x}) thin film by irradiation of photons using a KrF laser (λ = 248 nm) on an ammonium heptamolybdate ($(NH_4)_6Mo_7O_{24}\cdot 4H_2O$) precursor layer is demonstrated. The laser-assisted synthesis is simple, and can be conducted in an ambient atmosphere without damaging the underlying bottom electrode and plastic substrate. The exposure time (30 ns) is extremely short compared to thermal annealing (>3 min). Because the high-energy photons are absorbed by the MoO_3 layer and provide the activation energy for the reaction, the hydrogen atoms that dissociate from the ammonium molecules bond to the MoO_3; this process yields a H_yMoO_{3-x} thin-film. By controlling the laser energy, the stoichiometry of the H_yMoO_{3-x} layer can be manipulated to simultaneously obtain advantageous electrical properties of both high work function (5.6 eV) and electrical conductivity (9.9 μS cm^{-1}). The H_yMoO_{3-x} hole transport layer (HTL) is successfully demonstrated on flexible top-illuminated PTB7:PCBM organic solar cells (OSCs). This OSC has good mechanical flexibility, and 75% higher short-circuit current than the device with a PEDOT:PSS HTL. Finite-domain time-difference simulations were conducted to verify the enhancement of the photocurrent. The thin layer of H_yMoO_{3-x} was proven to be suitable for the microcavity condition which allows a resonant wavelength match to the PTB7:PCBM active layer.

Received 9th December 2015
Accepted 5th February 2016

DOI: 10.1039/c5ta10032a

www.rsc.org/MaterialsA

1. Introduction

Transition metal oxides (TMOs) have possible applications as the hole transport layer (HTL) among various charge transport materials[1–4] in optoelectronic devices such as organic light-emitting diodes,[6] organic solar cells (OSCs)[5–8] and perovskite solar cells.[9] Among TMOs, molybdenum oxide (MoO_3) is a promising candidate because of its transparency, air stability, and high work function (WF).[10–27] In the early stages of OSC research, vacuum-deposition was conducted for the fabrication of MoO_3 thin-films. However, as a large-area and low-cost roll-to-roll (R2R) fabrication has attracted attention for practical applications, a number of attempts have been conducted to obtain solution-processed MoO_3 as a HTL in OSCs.[10–18] Among the various properties of MoO_3, good electrical conductivity is needed for the HTL. Oxygen vacancies play a key role in obtaining the conductivity of the MoO_3 layer. Electrons fill up to the d-orbital, called gap states, as oxygen vacancies are produced. The occupied gap states make the Fermi level move near to the conduction band, thereby leading to an n-type semiconductor with increased electrical conductivity (σ). Thus, finding an easy way to create oxygen vacancies in solution-processed MoO_3 is critical to realize conducting MoO_3 for OSCs. The thermal annealing of ammonium molybdate at high temperature (>160 °C) has been considered to produce oxygen vacancies through the decomposition of MoO_3.[10–12] The performance of OSCs with thermally annealed ammonium molybdate was better than that of devices using poly(ethylenedioxythiophene):poly(styrenesulfonate) (PEDOT:PSS). However, the high-temperature heat treatment not only caused a severe aggregation but also damages the plastic substrate on which flexible OSCs are fabricated.[10,12] In order to reduce the annealing temperature (<120 °C) to protect the plastic substrate, several low-temperature precursors and processing methods have been conducted.

One method is to use hydrogen molybdenum bronzes, synthesized by dissolving Mo powder in hydrogen peroxide at room temperature.[14–16] The other method is to use ammonium heptamolybdate as an inexpensive precursor for low-temperature processing (100 °C).[17,18] These methods, however, require long processing times to obtain conductivity, leading to restraint from the employment of R2R processes for OSCs. Furthermore, it is hard to implement a micro-pattern on the solution-processed MoO_3 due to several steps in patterning for the implementation of devices.

In this paper, a low-temperature, and ultrafast method to produce solution-processed MoO_3 is demonstrated using KrF laser (λ = 248 nm, 5.0 eV) irradiation. The laser provides advantages because patterning can be simultaneously achieved by direct writing. High-density monochromatic photons

POSTECH, Material Science & Engineering, Pohang, Republic of Korea. E-mail: jllee@postech.ac.kr

† Electronic supplementary information (ESI) available. See DOI: 10.1039/c5ta10032a

are absorbed by an ammonium heptamolybdate ($(NH_4)_6Mo_7O_{24}\cdot 4H_2O$) thin-film and rapidly activate the reaction between ammonium molecules and MoO_3. This solid-state chemical reaction occurs in 30 ns. The laser energy changes the stoichiometry and electronic band structure of the solution-processed MoO_3 film, thereby resulting in both a high WF = 5.6 eV and high σ = 9.9 μS cm^{-1}. When the laser-assisted reaction is conducted for the preparation of HTLs in PTB7:PCBM-based OSCs, the annealing time is shortened by 10^9 times that of the conventional thermal annealing process. Moreover, the laser-irradiated MoO_3 HTL is proven to be effective in light trapping in the flexible top-illuminated OSCs, thereby resulting in a short-circuit current enhancement by 75% compared to the device with PEDOT:PSS. This flexible OSC showed no change in photo conversion efficiency (PCE) after 5000 bending cycles at a bending radius of 0.48 cm.

2. Experimental

2.1. Preparation of the MoO_3 solution

The MoO_3 solution was prepared by dissolving ammonium molybdate tetrahydrate ($(NH_4)_6Mo_7O_{24}\cdot 4H_2O$, Aldrich, 99.98%, 0.1 g) in 100 ml of deionized water.

2.2. Fabrication of PTB7:PCBM organic solar cells

Glass coated with ITO (150 nm thick, ~10 Ω sq^{-1}) was used as the starting substrate. It was treated using UV-ozone for 15 min followed by coating with the MoO_3 solution at 4000 rpm for 40 s. The resulting MoO_3 thin-film was irradiated at laser energies of 120, 240, 400 or 600 mJ cm^{-2}, using a KrF excimer laser (λ = 248 nm, frequency = 2 Hz, size = 0.25 cm^2). To fabricate the control device, a PEDOT:PSS layer was spin-coated at 3000 rpm for 30 s, then dried at 120 °C for 10 min. After samples were coated with the HTL, they were transferred to an N_2-filled glove box (<0.1 ppm O_2 and H_2O). PTB7 (purchased from 1-materials) was dissolved in chlorobenzene to make a 10 mg ml^{-1} solution, then blended with $PC_{70}BM$ (2 : 3 w : w). The blend was spin-coated (1600 rpm, 30 s) on top of the HTL. The thickness of the active layer was 80 nm as measured using an Alpha step 500 surface profiler. The cathode consisted of BCP (15 nm) coated with Ag (120 nm), which was deposited using a thermal evaporation method at a base pressure of 2 × 10^{-6} Torr.

2.3. Fabrication of flexible top-illuminated organic solar cells

Reflective Ag (120 nm) and ITO (20 nm) were deposited on the PES film by radio-frequency sputtering under a base pressure of 1 × 10^{-6} Torr. The films were treated with UV-ozone for 10 min, then coated with MoO_3 solution. The resulting MoO_3 layer was exposed to the laser with an energy of 240 mJ cm^{-2}. After the HTL was applied, the active layer of PTB7:PCBM was coated by spin coating. The devices were dried on a hot plate in a glove box at 80 °C for 10 min. The transparent cathode (BCP (15 nm)/Ag (12 nm)/MoO_3 (40 nm)) was deposited using thermal evaporation at a base pressure of 2 × 10^{-6} Torr.

2.4. Optical simulation

The finite-domain time-difference (FDTD) simulation (fullwave) was performed for numerical analysis of the light absorption and field distribution in the polymer solar cells. The side-wall of the photo-detector was composed of a perfect mirror and the grid size was fixed to 2 nm.

2.5. Characterization

The MoO_3 solution was spin-coated on the silicon substrate, followed by measuring of the thickness using a spectroscopic ellipsometer. The measured data was fitted using the Lorentz function, thereby resulting in a thickness of 3 nm. The FT-IR spectra were measured using a Bruker IFS 66v FT-IR spectrometer. The X-ray photoelectron spectroscopy (XPS) and ultraviolet photoelectron spectroscopy (UPS) were conducted on the 4D beam line at the Pohang Accelerator Laboratory with a base pressure of 5 × 10^{-10} Torr. AFM images were obtained in tapping mode on a Veeco Nanoscope III. An ITO (150 nm)/H_yMoO_{3-x}/Ag (120 nm) structure was fabricated for the measurement of electrical conductivity of H_yMoO_{3-x}. The conductivity was averaged over 40 samples for each of the treatment conditions. The *J–V* curves were measured under air ambient using a Keithley 2400 source measurement unit. The photocurrent was measured under AM 1.5 G 100 mW cm^{-2} illumination from an Oriel 150 W solar simulator. The light intensity was determined using a mono-silicon detector calibrated by the U.S. National Renewable Energy Laboratory (NREL). The incident photon to current efficiency (IPCE) was measured using a QEX10 Solar Cell Quantum Efficiency Measurement System (PV Measurements, Inc.). The integral of the IPCE curve measured under air mass 1.5 of the solar irradiance spectrum is

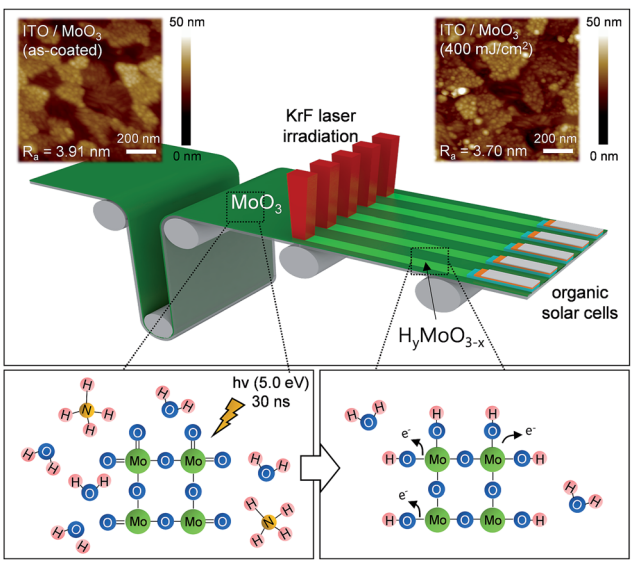

Fig. 1 Schematic illustration of the laser-assisted synthesis of the hydrogenated MoO_3 hole transport layer for flexible organic solar cells. Inset: atomic force microscope images of MoO_3 and laser-irradiated MoO_3.

a little smaller than the measured J_{sc} because the IPCE measurement cannot measure the wavelength below 400 nm.

3. Results and discussion

3.1. Reduction mechanism and chemical composition

The reaction of solution-processed ammonium heptamolybdate ($(NH_4)_6Mo_7O_{24}\cdot 4H_2O$) (Fig. 1) involves the coating of a solution-processed MoO_3 layer onto an ITO-deposited substrate, followed by irradiation using the KrF excimer laser. Due to the relatively small bandgap (3.3 eV) of the MoO_3 layer,[14] the incoming photons are absorbed and heat is generated by the non-radiative recombination of electron–hole pairs. This thermal energy rapidly activates the reaction between MoO_3 and surrounding NH_4^+ molecules. The surface morphology of the as-coated MoO_3 layer and laser-irradiated MoO_3 layers (Fig. 1, inset) have a similar root mean squared roughness of 3.91 nm and 3.70 nm, respectively. However, when the substrate is irradiated with high energy of 600 mJ cm^{-2}, cracks form in the ITO layer due to thermal shock (Fig. S1†). These cracks significantly increase the sheet resistance of the ITO electrode from 8 Ω sq^{-1} to 120 Ω sq^{-1}. The MoO_3 layers spin-coated on the ITO electrode have high optical transmittance ~84% regardless of laser irradiation (Fig. S2†); *i.e.*, the irradiation did not affect its optical properties.

To identify the structure of the MoO_3 thin-film, we performed Fourier transform infrared (FTIR) spectroscopy on several MoO_3 samples after treatment using laser irradiation or thermal annealing (Fig. 2a). The as-coated MoO_3 layer showed two distinct absorption bands at 949 cm^{-1} and 883 cm^{-1}. The band at 949 cm^{-1} is assigned to the stretching vibration of terminal oxygen (νO═Mo). The peak at 883 cm^{-1} is attributed to the Mo–O–Mo vibrations of Mo^{6+} for the stoichiometric MoO_3.[28–30] When the MoO_3 layer was irradiated with photons with mild energy (120 mJ cm^{-2}), a new band at 1074 cm^{-1} and broad band at 1120–1350 cm^{-1} appeared, due to the vibration

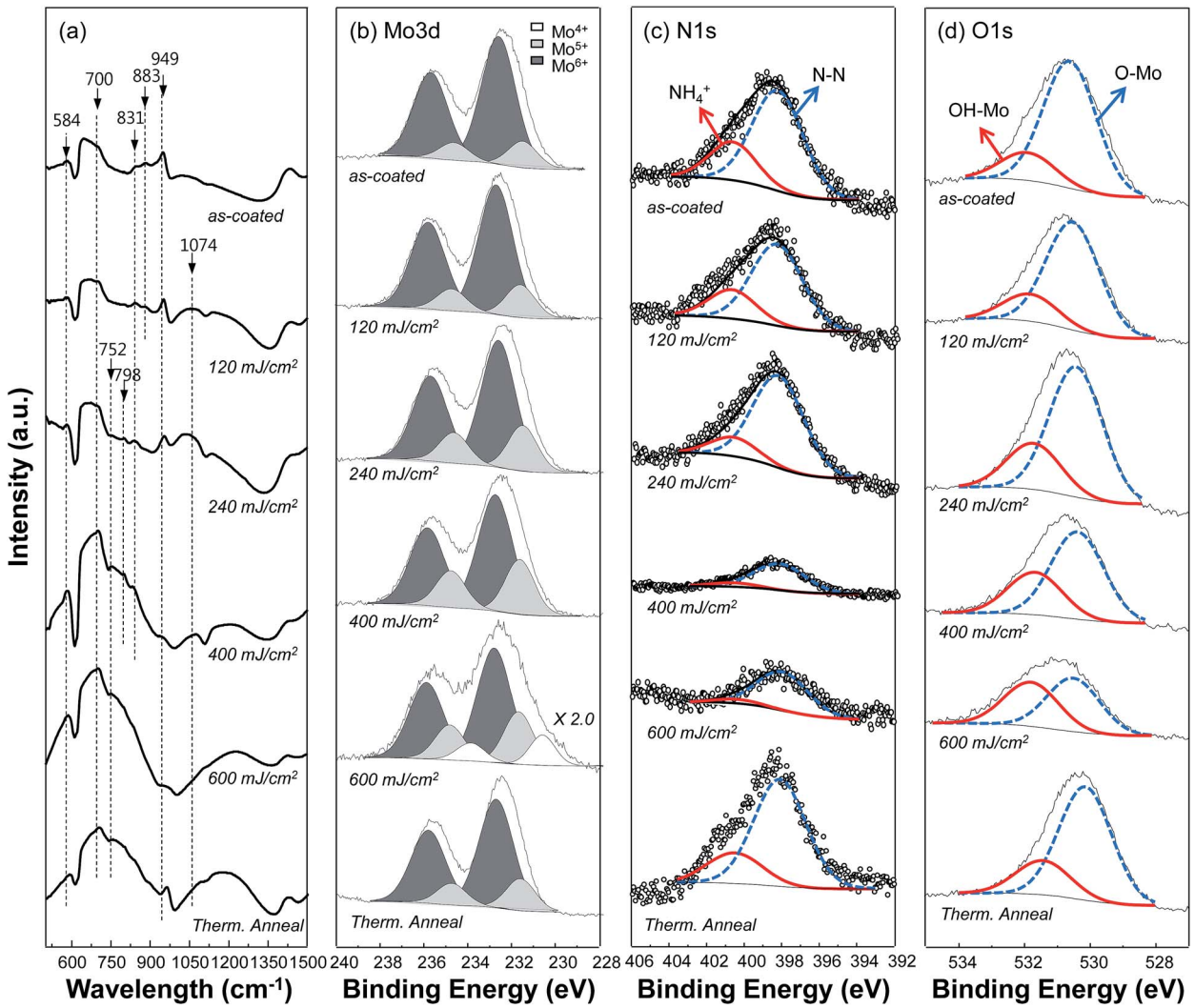

Fig. 2 (a) FT-IR spectra, (b) Mo3d, (c) N1s and (d) O1s XPS spectra of the as-coated, laser-irradiated and thermally-annealed MoO_3 layers. The precursor concentration of MoO_3 solution was 0.1 wt% and the measured thickness was 3 nm.

Table 1 Summary of atomic compositions of MoO_3 for various laser energies and thermal annealing

	Mo3d			O1s		N1s	
Laser energy (mJ cm^{-2})	Mo^{6+}	Mo^{5+}	Mo^{4+}	O–Mo	OH–Mo	N–N	NH^{4+}
As-coated	88%	12%	0%	91%	9%	72%	28%
120	88%	12%	0%	89%	11%	74%	26%
240	83%	17%	0%	86%	14%	83%	17%
400	79%	21%	0%	81%	19%	87%	13%
600	68%	21%	11%	67%	33%	91%	9%
Thermal annealing	92%	8%	0%	91%	9%	81%	19%

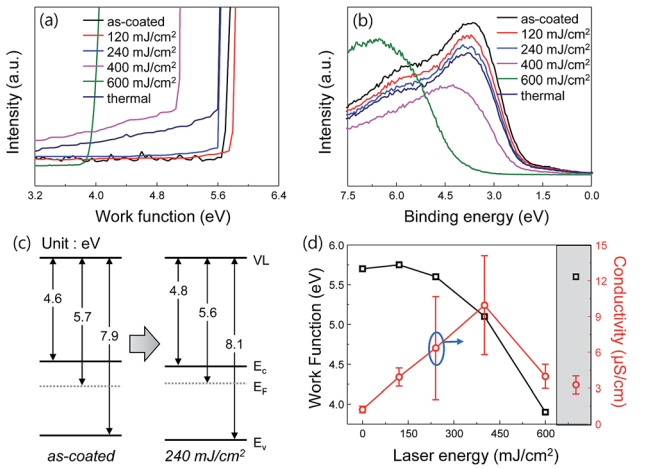

Fig. 3 (a) Secondary electron emission spectra and (b) valence band spectra of MoO_3 layers. (c) Schematic energy band diagram of as-coated and laser-irradiated MoO_3 layers. (d) Work function and electrical conductivity *vs.* laser energy. Shaded region: results of the thermally annealed sample.

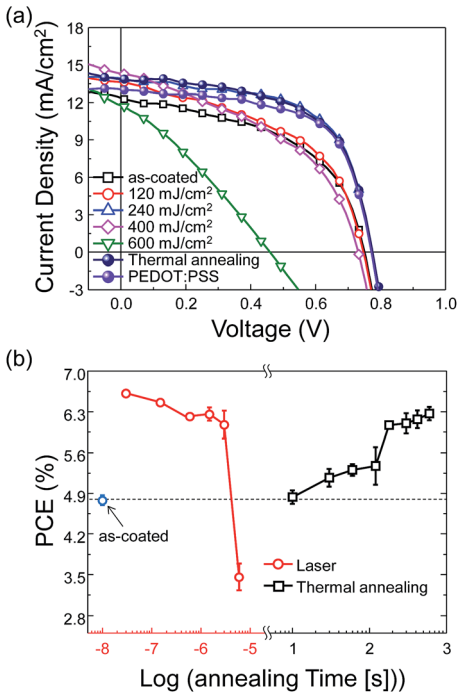

Fig. 4 (a) *J–V* characteristics of PTB7:PCBM bulk-heterojunction solar cells with MoO_3 hole transport layers. (b) PCE of OSCs as a function of annealing time of MoO_3. The laser energy was 240 mJ cm^{-2} for the laser-assisted reaction and the temperature was 150 °C for thermal annealing.

mode of Mo–O–H and deformation mode of Mo–O–H bonds (δMo–OH), respectively.[28–30] As the laser energy increased, the bands of the terminal oxygen (νO=Mo, 949 cm^{-1}) and Mo–O–Mo (831 and 883 cm^{-1}) disappeared while the intensity of the band between 752 and 798 cm^{-1} (νMo–O) and the band above 1120 cm^{-1} (Mo–O–H) increased. The thermally annealed MoO_3 layer prepared at 150 °C for 10 min on hot plate, exhibited the band of terminal oxygen at 949 cm^{-1}, which is evidence that less Mo was reduced than in the sample treated by laser irradiation at 240 mJ cm^{-2}. We propose that the laser-assisted reaction of MoO_3 proceeds as follows: excess hydrogen atoms produced by the decomposition of NH_4^+ react with MoO_3, thereby converting the terminal oxygen (Mo=O) to hydroxyl groups (Mo–OH). This reaction reduces the Mo^{6+} to Mo^{5+} or Mo^{4+}.

In order to characterize the stoichiometric composition of MoO_3 in detail, the Mo3d spectrum was measured using synchrotron X-ray photoelectron spectroscopy (XPS) (Fig. 2b) and the atomic compositions of laser-irradiated and thermally-annealed MoO_3 thin films were determined (Table 1). In a molybdenum oxide, the binding energies are centered at 233.0 eV for Mo^{6+}, at 231.8 eV for Mo^{5+}, and at 230.8 eV for $Mo4^+$. Deconvolution of the Mo3d spectrum reveals that they are fitted by doublets in the form of Gaussian functions.[31,32] As the laser energy increased, the intensity of the Mo^{6+} peak decreased and the reduced state of the Mo^{5+} peak became apparent. Particularly, when the MoO_3 layer was irradiated with high energy of 600 mJ cm^{-2}, the highly-reduced Mo^{4+} appeared. These Mo^{4+} ions resulted from an increased number of Mo–OH bonds[15] and the direct bonds of hydrogen atoms with Mo ions.[33]

The N1s XPS spectra (Fig. 2c) were deconvoluted to two peaks; one of N–N (398.5 eV) and one of NH_4^+ (401 eV).[18] The N–N bonds are associated with surface-adsorbed N; the NH_4^+ represents the ammonium functional groups in the solution-processed MoO_3 thin-film. As the laser energy increased, the NH_4^+ peak gradually disappeared. We believe that the ammonium molecules at the surface decomposed to NH_3 gas and H^+ during laser irradiation.[34] The H^+ reacts with double-bonded terminal oxygen atoms in MoO_3. The reaction produces hydroxyl groups (–OH) in the MoO_3 thin-film as indicated in the

O1s XPS spectra (Fig. 2d). The XPS O1s spectra of the as-coated MoO_3 shows a peak at 530.6 eV, which is assigned to the Mo–O bond.[17] As the laser energy was increased, an extra peak of hydroxyl groups (–OH) at the binding energy of 532 eV increased gradually. These XPS results indicate that the MoO_3 layer was hydrogenated to form hydrogenated molybdenum oxide (H_y-MoO_{3-x}). In the thermally annealed sample, the Mo3d, N1s and O1s spectra show a similar atomic composition to the MoO_3 thin films that had been irradiated at 120 mJ cm^{-2}.

3.2. Electrical properties of reduced MoO_3

The secondary electron emission spectra (Fig. 3a) show the WF of the MoO_3 thin-film after irradiation at various laser energies, or after thermal annealing. As the laser energy increased, the WF decreased because many of the Mo cations were reduced to Mo^{5+} and Mo^{4+}, which have a small electronegativity.[31,32] The valence band maximum (VBM) was located at 2.2 eV for the as-coated MoO_3 thin-film, but gradually increased to 4.0 eV in the sample with that had been irradiated at 600 mJ cm^{-2} (Fig. 3b).

The band diagrams of the as-coated and laser-irradiated MoO_3 thin films (Fig. 3c) were determined from the secondary electron emission spectra and valence band spectra. The WF of MoO_3 decreased and the valence bands shifted to higher binding energy as the laser energy increased; as a result, the Fermi level (E_F) of the reduced MoO_3 shifted toward the conduction band edge (E_c), thereby resulting in an n-type doping effect. The shift of E_F is attributed to the increased number of free electrons. The WF varied quadratically with laser energies; it was highest (5.75 eV) at 120 mJ cm^{-2} and lowest (3.9 eV) at 600 mJ cm^{-2} (Fig. 3d). In contrast, the average electrical conductivity increased from 1.2 μS cm^{-1} to 9.9 μS cm^{-1} at 400 mJ cm^{-2}. The samples treated at 240 mJ cm^{-2} and 400 mJ cm^{-2}, had a higher average electrical conductivity than the thermally annealed samples. In the sample treated at 600 mJ cm^{-2}, the electrical conductivity decreased due to degradation of the ITO electrode.

3.3. Ultrafast reaction of the MoO_3 hole transport layer for organic solar cells

In order to demonstrate the laser-irradiated MoO_3 layer as a hole transport layer (HTL) in organic solar cells, PTB7:PCBM bulk-heterojunction solar cells were fabricated on ITO-coated glass substrates. Current density–voltage (J–V) curves (Fig. 4a) and device parameters (Table 2) were obtained for devices with as-coated MoO_3, laser-irradiated MoO_3, thermally annealed MoO_3, and PEDOT:PSS. The device with the as-coated MoO_3 had an open circuit voltage (V_{oc}) = 0.75 V, short-circuit current (J_{sc}) = 12.5 mA cm^{-2}, fill factor (FF) = 50.3% and low PCE = 4.7%. After laser irradiation (240 mJ cm^{-2}) of the MoO_3 layer, the PCE increased to the maximum value of 6.6%, which was higher than the PCE of the control devices with PEDOT:PSS HTL (PCE = 6.3%) and the device with thermally-annealed MoO_3 (PCE = 6.4%). The enhancement of PCE is mainly ascribed to the increases in J_{sc} and FF, which occurred as a consequence of the increase in electrical conductivity. When the laser energy of 400 mJ cm^{-2} is used, the PCE decreased to 4.6% due to a low WF (5.1 eV). When the laser energy increased to 600 mJ cm^{-2}, the PCE further decreased to 1.6%. This is due to the WF being reduced to 3.9 eV and an excess of hydrogen ions are produced to form Mo–H bonds, having a role in trapping the charge carriers.[33]

To compare the reaction time of the laser-assisted reaction and conventional thermal annealing, OSCs were fabricated with precursors annealed for various durations (Fig. S3 and Table S1†). The annealing time of the laser-assisted reaction was controlled by adjusting the number of laser pulses with a frequency of 2 Hz and a pulse duration of 30 ns. Thermal annealing was conducted at 150 °C on a hot plate. When the MoO_3 layer was irradiated with energy of 240 mJ cm^{-2}, the efficiency of the OSCs drastically increased and reached a maximum PCE value of 6.6% within 30 ns (Fig. 4b, red). In contrast, the thermal annealing of MoO_3 slowly increased the efficiency of the OSCs (Fig. 4b, black). The annealing duration required to achieve an efficiency of 6.1% was 3 min. These results verify that the laser-assisted reaction dramatically reduces the fabrication time compared to conventional thermal annealing. The structure of the MoO_3 changes with annealing time (Fig. S4†).

3.4. Flexible top-illuminated organic solar cells

Flexible top-illuminated PTB7:PCBM-based organic solar cells were fabricated on flexible polyethylene sulfone (PES) films; the device structure of the top-illuminated solar cell was: PES film/

Table 2 Photovoltaic characteristics of the devices with various HTLs. The illumination condition used for the measurements was AM 1.5 G 100 mW cm^{-2}

HTL	V_{oc} (V)	J_{sc} (mA cm^{-2})	FF (%)	PCE (%)	WF (eV)	Average σ (μS cm^{-1})
As-coated	0.75	12.5	50.3	4.72	5.7	1.2
120 mJ cm^{-2}	0.75	13.7	49.8	5.12	5.75	3.9
240 mJ cm^{-2}	0.77	13.9	61.2	6.55	5.6	6.3
400 mJ cm^{-2}	0.73	14.3	44.4	4.63	5.1	9.9
600 mJ cm^{-2}	0.45	11.9	30.2	1.62	3.9	4.0
Thermal annealing	0.77	13.8	60.2	6.43	5.6	3.3
PEDOT:PSS	0.77	13.0	63.2	6.32	—	—

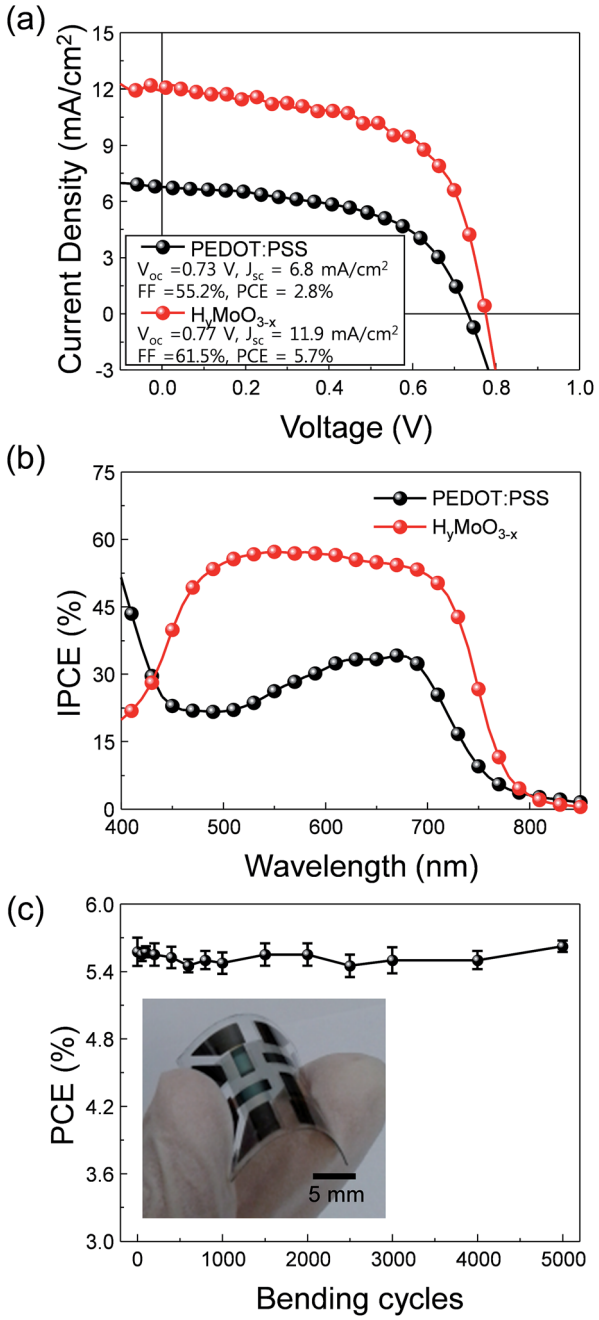

Fig. 5 (a) J–V curves and (b) IPCE spectra of flexible top-illuminated OSCs. Device structure of flexible OSCs: PES film/Ag (120 nm)/ITO (20 nm)/HTL/PTB7:PCBM (80 nm)/BCP (15 nm)/Ag (12 nm)/MoO_3 (40 nm). (c) Change in photo-conversion efficiency (PCE) by bending cycles at a radius of 0.48 cm.

Ag (120 nm)/ITO (20 nm)/HTL/PTB7:PCBM (80 nm)/BCP (15 nm)/Ag (12 nm)/MoO_3 (40 nm). The thin ITO (20 nm) was inserted between the Ag layer and the solution-processed HTL to allow wetting of the MoO_3 and PEDOT:PSS solution on the hydrophobic Ag reflector. The device with H_yMoO_{3-x} had a higher J_{sc}, FF and V_{oc} than the device based on PEDOT:PSS (Fig. 5a). The flexible OSCs with H_yMoO_{3-x} had a much higher PCE = 5.7% than the control device with PEDOT:PSS (PCE = 2.8%). The high efficiency of OSCs with H_yMoO_{3-x} can be attributed to its higher short-circuit current (11.9 mA cm^{-2}) compared to that of the device with PEDOT:PSS (6.8 mA cm^{-2}). The incident photon-to-current efficiency (IPCE) (Fig. 5b) was measured to determine the reason for the efficiency increase. The OSCs fabricated with the PEDOT:PSS HTL had a small IPCE, but the device with the H_yMoO_{3-x} layer generated a large amount of photocurrent in the visible spectrum region ($400 \leq \lambda \leq 800$ nm). This result demonstrates that the thin H_yMoO_{3-x} layer (3 nm) absorbs light much more efficiently than the thick PEDOT:PSS layer (40 nm). The mechanical flexibility of the OSCs was characterized in a bending cycle test. The flexible top-illuminated OSCs fabricated on the PES film did not lose efficiency even after 5000 bending cycles with a radius of 0.48 cm (Fig. 5c).

The contour of light absorption in top-illuminated OSCs was characterized by optical simulation to verify the effect of thin HTLs on the increase in light absorption. Assuming that the light strikes the surface in the normal direction, an optical simulation was conducted using the finite-difference time-domain (FDTD) simulation. When the PEDOT:PSS was used as the HTL in OSCs (Fig. 6a), the wavelength at which light absorption was highest positions at a long wavelength (720 nm), and the contour diverged from the center of the PTB7:PCBM active layer. The contour of external quantum efficiency (EQE) is plotted by multiplying absorption and internal quantum efficiency. Because the peak wavelength of the EQE (710 nm) is far from the absorption region of the active layer (400–700 nm) (Fig. 6a) and the IQE (Fig. S5†) rapidly drops above 700 nm, OSCs with PEDOT:PSS cannot efficiently generate a photocurrent from the absorbed photons, resulting in a low EQE. In contrast, the OSCs with the H_yMoO_{3-x} layer (Fig. 6b) strongly absorbed photons on a broad range of the visible spectrum (500 nm < λ < 700 nm) where both the absorbance and IQE of PTB7:PCBM are simultaneously large. The peak of the EQE (610 nm) is positioned at the center of the PTB7:PCBM active layer. Therefore, the calculated EQE of the devices with H_yMoO_{3-x} is larger than the cells with PEDOT:PSS. The large difference in the EQE of these two devices results from an optical microcavity. Because the distance between the top semi-transparent Ag layer and the bottom reflective Ag electrode determines the resonant wavelength of the microcavity in the active layer, the HTL (PEDOT:PSS or H_yMoO_{3-x}) plays a role as an optical spacer, which affects light absorption in the device. The low efficiency of OSCs with PEDOT:PSS can be explained by the long distance between two Ag reflectors. In order to fit the resonant wavelength of OSCs with PEDOT:PSS to the center of the absorbance spectrum of PTB7:PCBM, the thickness of the active layer should be reduced to 45 nm (Fig. S6†), resulting in broadband light absorption. However, the total absorption of light was decreased because the thin PTB7:PCBM layer (45 nm) is not enough to absorb incident photons compared to the thick PTB7:PCBM layer (80 nm). This provides evidence that the light absorption in OSCs with a PEDOT:PSS layer could not overcome that in top-illuminated OSCs with a H_yMoO_{3-x} one, even though the microcavity was optimized.

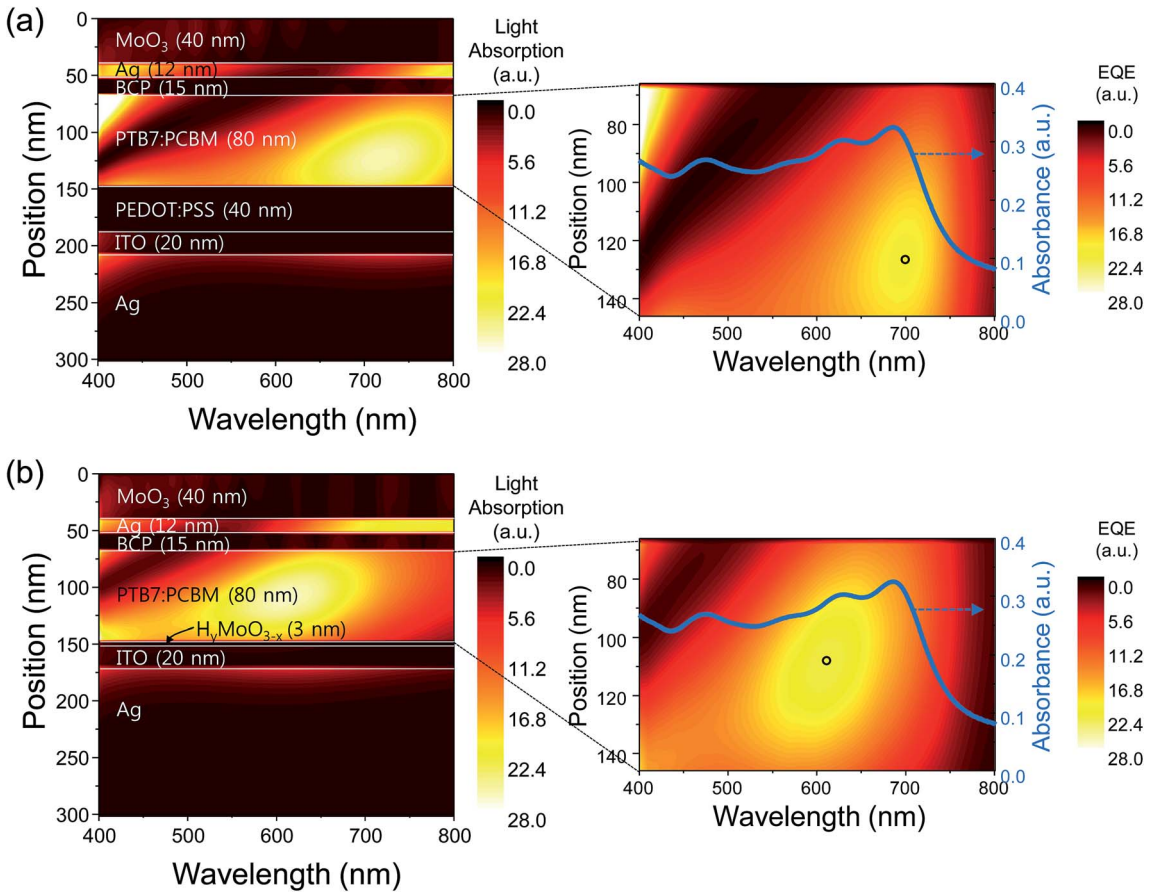

Fig. 6 2-Dimensional contour of light absorption and calculated EQEs in top-illuminated OSCs with (a) PEDOT:PSS and (b) H_yMoO_{3-x} HTLs. Absorbance of PTB7:PCBM is plotted on the right figure.

4. Conclusions

In summary, an ultrafast laser-assisted reaction of hydrogenated molybdenum oxide (H_yMoO_{3-x}) thin films was demonstrated. The stoichiometry of the H_yMoO_{3-x} layer was controlled by laser energy, thereby resulting in beneficial electronic properties such as high WF (5.6 eV) and electrical conductivity (9.9 μS cm^{-1}). When the laser-assisted reaction was conducted for the preparation of hole transport layers for organic solar cells, the annealing time was reduced by a factor of 10^9 compared to conventional thermal annealing. The H_yMoO_{3-x} HTL was effective not only for charge transport but also for light trapping in flexible top-illuminated OSCs. A flexible device with H_yMoO_{3-x} exhibited enhancement of the short-circuit current by 75% compared to the device with PEDOT:PSS. The optical simulation verifies that the thin layer of H_yMoO_{3-x} (3 nm) is effective for light absorption in the microcavity, where the resonant wavelength matches with the absorption band of PTB7:PCBM. This laser-assisted low-temperature and ultrafast reaction method can be conducted for other transition metal oxides, and is suitable for R2R fabrication of flexible electronics.

Acknowledgements

This work was supported by the National Research Foundation of Korea (NRF) grant funded by the Korea government (MSIP) (No. NRF-2013R1A2A2A01069237).

References

1 K.-G. Lim, S. M. Park, H. Y. Woo and T.-W. Lee, *ChemSusChem*, 2015, **8**, 3062.
2 D.-H. Kim, K.-G. Lim, J. H. Park and T.-W. Lee, *ChemSusChem*, 2012, **5**, 2053.
3 M.-R. Choi, T.-H. Han, K.-G. Lim, S.-H. Woo, D. H. Huh and T.-W. Lee, *Angew. Chem., Int. Ed.*, 2011, **50**, 6274.
4 H. J. Bolink, E. Coronado, J. Orozco and M. Sessolo, *Adv. Mater.*, 2009, **21**, 79.
5 Z. He, C. Zhong, S. Su, M. Xu, H. Wu and Y. Cao, *Nat. Photonics*, 2012, **6**, 591.
6 G. Li, R. Zhu and Y. Yang, *Nat. Photonics*, 2012, **6**, 153.
7 S. Chen, J. R. Manders, S.-W. Tsang and F. So, *Adv. Mater.*, 2012, **22**, 24202.
8 V. Shrotriya, G. Li, Y. Yao, C.-W. Chu and Y. Yang, *Appl. Phys. Lett.*, 2006, **88**, 073508.

9 J.-Y. Jeng, K.-C. Chen, T.-Y. Chiang, P.-Y. Lin, T.-D. Tsai, Y.-C. Chang, T.-F. Guo, P. Chen, T.-C. Wen and Y.-J. Hsu, *Adv. Mater.*, 2014, **24**, 4107.
10 F. Liu, S. Shao, X. Guo, Y. Zhao and Z. Xie, *Sol. Energy Mater. Sol. Cells*, 2010, **94**, 842.
11 J. Meyer, R. Khalandovsky, P. Gorrn and A. Kahn, *Adv. Mater.*, 2011, **23**, 70.
12 C. Girotto, E. Voroshazi, D. Cheyns, P. Heremans and B. P. Rand, *ACS Appl. Mater. Interfaces*, 2011, **3**, 3244.
13 S. R. Hammond, J. Meyer, N. E. Widjonarko, P. F. Ndione, A. K. Sigdel, A. Garcia, A. Miedaner, M. T. Lloyd, A. Kahn, D. S. Ginley, J. J. Berry and D. C. Olson, *J. Mater. Chem.*, 2012, **22**, 3249.
14 F. Xie, W. C. H. Choy, C. Wang, X. Li, S. Zhang and J. Hou, *Adv. Mater.*, 2013, **25**, 2051.
15 M. Vasilopoulou, A. M. Douvas, D. G. Georgiadou, L. C. Palilis, S. Kennou, L. Sygellou, A. Soultati, I. Kostis, G. Papadimitropoulos, D. Davazoglou and P. Argitis, *J. Am. Chem. Soc.*, 2012, **134**, 16178.
16 A. Soultati, A. M. Douvas, D. G. Georgiadou, L. C. Palilis, T. Bein, J. M. Feckl, S. Gardelis, M. Fakis, S. Kennou, P. Falaras, T. Stergiopoulos, N. A. Stathopoulos, D. Davazoglou, P. Argitis and M. Vasilopoulou, *Adv. Energy Mater.*, 2014, **4**, 1300896.
17 S. Murase and Y. Yang, *Adv. Mater.*, 2012, **24**, 2459.
18 J. Griffin, A. J. Pearson, N. W. Scarratt, T. Wang, D. G. Lidzey and A. R. Buckley, *Org. Electron.*, 2014, **15**, 692.
19 J. J. Jasieniak, J. Seifter, J. Jo, T. Mates and A. J. Heeger, *Adv. Funct. Mater.*, 2012, **22**, 2594.
20 Y.-J. Lee, J. Yi, G. F. Gao, H. Koerner, K. Park, J. Wang, K. Luo, R. A. Vaia and J. W. P. Hsu, *Adv. Energy Mater.*, 2012, **2**, 1193.
21 W. J. Dong, G. H. Jung and J.-L. Lee, *Sol. Energy Mater. Sol. Cells*, 2013, **116**, 94.
22 C. Yao, X. Xu, J. Wang, L. Shi and L. Li, *ACS Appl. Mater. Interfaces*, 2013, **5**, 1100.
23 K. Zilberberg, H. Gharbi, A. Nehrendt, S. Trost and T. Riedl, *ACS Appl. Mater. Interfaces*, 2012, **4**, 1164.
24 W. Qiu, A. Hadipour, R. Muller, B. Conings, H.-G. Boyen, P. Heremans and L. Froyen, *ACS Appl. Mater. Interfaces*, 2014, **6**, 16335.
25 J. Wang, J. Zhang, B. Meng, B. Zhang, Z. Xie and L. Wang, *ACS Appl. Mater. Interfaces*, 2015, **7**, 13590.
26 X. Li, F. Xie, S. Zhang, J. Hou and W. C. H. Choy, *Light: Sci. Appl.*, 2015, **4**, e273.
27 H. Cheng, T. Kamegawa, K. Mori and H. Yamashita, *Angew. Chem., Int. Ed.*, 2014, **53**, 2910.
28 T. Weber, J. C. Muijsers, J. H. M. C. van Wolput, C. P. J. Verhagen and J. W. Niemantsverdriet, *J. Phys. Chem.*, 1996, **100**, 14144.
29 M. Dhanasankar, K. K. Purushothaman and G. Muralidharan, *Appl. Surf. Sci.*, 2011, **257**, 2074.
30 T. H. Chiang and H. C. Yeh, *Materials*, 2013, **6**, 4609.
31 M. T. Greiner, L. Chai, M. G. Helander, W.-M. Tang and Z.-H. Lu, *Adv. Funct. Mater.*, 2013, **23**, 215.
32 M. T. Greiner, L. Chai, M. G. Helander, W.-M. Tang and Z.-H. Lu, *Adv. Funct. Mater.*, 2012, **22**, 4557.
33 I. Kostis, N. Vourdas, G. Papadimitropoulos, A. Douvas, M. Vasilopoulou, N. Boukos and D. Davazoglou, *J. Phys. Chem. C*, 2013, **117**, 18013.
34 P. Pichat, M.-N. Mozzanega and C. Hoang-Van, *J. Phys. Chem.*, 1988, **92**, 467.

